

Bistability of a helical filament confined on a cylinderZicong Zhou *Department of Physics, Tamkang University, 151 Ying-chuan, Tamsui 25137, Taiwan, ROC* (Received 8 September 2021; revised 30 December 2021; accepted 31 January 2022; published 14 February 2022)

The natural configuration of an intrinsically curved and twisted filament is uniquely a helix so that it can be referred to as a helical filament. We find that confining a helical filament on a cylinder can create a bistable state. When $c_0R = 0.5$, where c_0 is the intrinsic curvature of filament and R is the radius of cylinder, the phase diagram for the stability of a helix contains three regimes. Regime *I* has a small intrinsic twisting rate (ITR) and exhibits a bistable state which consists of two isoenergetic helices. In regime *II*, the filament has a moderate ITR and the bistable state consists of a metastable low-pitch helix and a stable nonhelix. In regime *III*, the helix is unstable, owing to a large ITR. A similar phenomenon occurs when $c_0R \sim 0.5$. Monte Carlo simulation confirms these conclusions and indicates further that there are bistable nonhelices in regime *III*. This bistable system offers a prospective green material since the wide range of parameters and distinctive configurations for bistable states favor its realization and application.

DOI: [10.1103/PhysRevE.105.024502](https://doi.org/10.1103/PhysRevE.105.024502)**I. INTRODUCTION**

A bistable material has two equilibrium states so can stay in either of two states and switch between them in a controllable way. Owing to this fantastic property, these materials have been widely used as memory, oscillators, multivibrators, or switches in sensing, information processing, spintronics, and smart materials. For instance, because of a low energy cost in keeping different colored state, bistable material is an idea choice for a display [1–4]. Therefore, to search for new bistable material and the property of new material have attracted considerable attentions for decades in material science. Meanwhile, understanding the conformational and mechanical properties of a filament is a significant issue owing to its crucial importance in either macroscopic objects such as pillars or microscopic objects such as nanotubes or biopolymers [5–16]. Moreover, confined materials are ubiquitous and crucial in various fields. A confined material is usually referred to as a material which cannot move freely in three-dimensional (3D) space so that it includes both one and two-dimensional (2D) materials [17] since these materials can be adsorbed on a substrate or confined on a chain or inside a nanotube. For instance, a single monolayer of graphene or 2D transition metal dichalcogenides can be exfoliated from multilayers or grown from solutions or obtained by depositing some molecules into a substrate [18–20]. However, many biopolymers in vivo are subjected to various constraints, such as being absorbed on some substrates or moving in a crowd environment or confined inside some cells [21–52]. MreB inside rod-shaped (cylindrical) bacteria gives such an example [35–52]. MreB and MreB homologs are actin homolog proteins and are found in all rod-shaped bacteria [36,40,42]. They play important roles in lots of cellular functions, such as the regulation of cell shape, chromosome segregation, determination of cell polarity, and organization of membranous

organelles [35,37,40,42]. In particular, MreB is essential to maintain the shape of a rod-like cell, as their disruption leads to cell rounding. It was reported that MreB filaments have a persistence length 5 to 10 times larger than bacterial cell size [35,41] so that the cell provides a strong constraint on MreB.

A confined material often exhibits significantly different property from that of the unconfined material. For instance, a 2D solar cell can have much higher efficiency than that of the bulk one. Another example is that MreB is intrinsically straight, i.e., free of external force its ground state configuration (GSC, or the configuration with the lowest energy) is a straight line. Indeed, MreB is straight when it is expressed within fission yeast [45]. However, within a cell, MreB can be either a helix or a ring [35–40,42,44,46–51]. Moreover, it has been reported that confining a helical filament on a plane yields a bistable system [53] so is considerably different from its 3D counterpart. Here a helical filament is referred to as an intrinsically curved and twisted filament since its natural or force-free GSC is uniquely a helix [10]. It is reasonable to expect that other forms of confinement can result in similar phenomenon and a helical filament confined on a cylinder is naturally a candidate worth of a close examination. In this system, in the limit of a zero radius (R) of cylinder, the filament must be straight. However, $c_0R \geq 1$ results in a natural helix with radius = R , where c_0 is the intrinsic curvature (IC) of the filament, since the confinement becomes futile. What will occur when $1 > c_0R > 0$? In this paper, we report that the competition and cooperation between intrinsic property and geometric constraint can bring about a new bistable material. Using variational technique and Monte Carlo simulation, we find that when $c_0R = 0.5$ and the twisting rigidity is greater than the bending rigidity, the filament can form a bistable state (BS) which consists of two isoenergetic helices or a metastable low-pitch helix and a stable nonhelix or two nonhelices. When

$c_0R \sim 0.5$ it still has a BS though two helices are no longer isoenergetic. It offers a prospective green material since to keep the filament staying in one of two configurations in a BS does not need external force, and a wide range in parameters for such a system make it easier be realized than a 2D system so is more practical.

The paper is organized as follows. In the next section we set up the elastic model for a helical filament. It follows a section to derive static equations, i.e., the equations to determine GSC of the filament, and find their helical solutions. In Sec. IV we derive stability criterion for helical configuration. In Sec. V we present analytical results for bistability. In Sec. VI we report results obtained from Monte Carlo simulation to support our analytical conclusions. Section VII completes the paper with conclusions and discussions.

II. MODEL

A. Continuous model

The configuration of a filament is determined by the shape of its centerline and the twist of its cross-section around the centerline. Denoting the arclength of centerline as s and the locus of centerline as $\mathbf{r}(s)$, the configuration of a filament in 3D space can be described by a triad of unit vectors $\{\mathbf{t}_i(s)\}_{i=1,2,3}$, where \mathbf{t}_1 and \mathbf{t}_2 are oriented along the principal axes of the cross-section, $\mathbf{t}_3 \equiv \dot{\mathbf{r}}$ is the tangent to the centerline and the symbol “ $\dot{\cdot}$ ” represents the derivative with respect to s [5–10]. The orientation of the triad is determined by the generalized Frenet equations $\dot{\mathbf{t}}_i = \boldsymbol{\omega} \times \mathbf{t}_i$ [5–10,54], where the vector $\boldsymbol{\omega} = (\omega_1, \omega_2, \omega_3)$ represents curvature and torsion parameters. Moreover, \mathbf{t}_i and $\boldsymbol{\omega}$ can be represented by Euler angles θ, ϕ , and ψ as [5–10,55]

$$\mathbf{t}_3 = (\sin \phi \sin \theta, -\cos \phi \sin \theta, \cos \theta), \quad (1)$$

$$\omega_1 = \sin \theta \sin \psi \dot{\phi} + \cos \psi \dot{\theta}, \quad (2)$$

$$\omega_2 = \sin \theta \cos \psi \dot{\phi} - \sin \psi \dot{\theta}, \quad (3)$$

$$\omega_3 = \cos \theta \dot{\phi} + \dot{\psi}. \quad (4)$$

The main advantage of using Euler angles is that it is relative easier to find some exact results, as we can see later.

In 3D space, the energy of an isotropic and uniform filament with finite intrinsic twisting rate (ITR = ω_{30}) and c_0 can be written as [5–10]

$$E = \int_0^L \mathcal{E} ds, \quad (5)$$

$$\mathcal{E} = \frac{k}{2}[(\omega_1 - \omega_{10})^2 + (\omega_2 - \omega_{20})^2] + \frac{k_3}{2}(\omega_3 - \omega_{30})^2, \quad (6)$$

where k is bending rigidity, k_3 is twisting rigidity, ω_{10} and ω_{20} are components of c_0 ($c_0 = \sqrt{\omega_{10}^2 + \omega_{20}^2}$), L is the total contour length and a constant so the filament is inextensible. This model is valid for both macroscopic and microscopic filaments and is often used to describe a semiflexible biopolymer. For instance, for a dsDNA at temperature $T = 298K$, $k/k_B T \approx 50$ nm, $k_3/k_B T \approx 75$ nm where k_B is the Boltzmann constant, and $\omega_{30} \approx 1.76$ nm⁻¹ [11,12]. The unique GSC of the model in 3D space is a helix with $\tan \theta = c_0/\omega_{30}$ and radius $R_h^0 = c_0/(c_0^2 + \omega_{30}^2)$ [9,10].

Equation (5) ignores external force or torque. Applying a torque (Γ) along the axis of filament yields an energy density $-\Gamma\omega_3$ [56]. But since $k_3/2(\omega_3 - \omega_{30})^2 - \Gamma\omega_3 = k_3/2[\omega_3 - (\omega_{30} + \Gamma/k_3)]^2 - (\omega_{30} + \Gamma/2k_3)\Gamma$, Γ plays a role of effective ω_{30} so we ignore it in calculation but it can be useful in application since Γ can be replaced by binding cross-section in two ends. Moreover, let $\omega_{10} = c_0 \cos \alpha_0$ and $\omega_{20} = c_0 \sin \alpha_0$, it is straightforward to show that α_0 adds only a constant in ψ so we also ignore α_0 henceforth.

Confining the filament on a cylinder applies a constraint on \mathbf{r} so $x = R(1 - \cos \phi)$ and $y = -R \sin \phi$ [56,57]. It follows $\dot{\phi} = \sin \theta/R$ [56,57] and \mathcal{E} can be rewritten as

$$\mathcal{E} = \frac{k}{2} \left[(\dot{\theta} - c_0 \cos \psi)^2 + \left(\frac{\sin^2 \theta}{R} - c_0 \sin \psi \right)^2 \right] + \frac{k_3}{2} \left(\dot{\psi} + \frac{\sin \theta \cos \theta}{R} - \omega_{30} \right)^2. \quad (7)$$

B. Discrete model

Using standard variational technique we can derive static equations for GSC and find their helical solutions exactly, as we will report in Sec. III. The static equations are nonlinear differential equations so they have multiple solutions and since it is very difficult to find the general solution, these exact results are not yet enough to decide GSC or helices may be only metastable. Moreover, the property of a microscopic filament may be sensitive to thermal fluctuation and the continuous model represents the limit of a long filament so that its conclusion may demand a correction for a short one.

To clarify these problems, we discretize the continuous model and perform Monte Carlo simulation. In discrete model, a filament consists of N straight and inextensible rods of length d_0 joined end to end. Replacing $\theta(s)$ by θ_i , $\psi(s)$ by ψ_i , $\dot{\theta}(s)$ by $\Delta\theta_i/d_0 \equiv (\theta_{i+1} - \theta_i)/d_0$, $\dot{\psi}(s)$ by $\Delta\psi_i/d_0 \equiv (\psi_{i+1} - \psi_i)/d_0$, the reduced energy becomes

$$E_T \equiv E/k_B T = \frac{1}{2} \sum_{i=1}^{N-1} [b(\Delta\theta_i - c_0 \cos \psi_i)^2 + b(\sin^2 \theta_i/R + c_0 \sin \psi_i)^2 + b_3(\Delta\psi_i + \sin \theta_i \cos \theta_i/R - \omega_{30})^2], \quad (8)$$

where $b \equiv k/d_0 k_B T$ and $b_3 \equiv k_3/d_0 k_B T$. We also scale the length by d_0 , i.e., let $d_0 = 1$ so $L = N$. In this convention, we can no longer let $R = 1$ so that to compare with the exact calculations, we need to replace c_0 by $c_0 R$ and ω_{30} by $\omega_{30} R$. In simulation we apply hinged-hinged boundary conditions, i.e., angles at both ends are free, so that the filament can switch freely among different configurations. We equilibrate every sample for 2×10^6 Monte Carlo steps (MCS) before performing average, and MCS for thermal average of a sample is up to 2×10^8 but the results are the same when MCS $\geq 10^7$. Moreover, the initial configuration of every sample is randomly set to avoid bias. The thermal average will be denoted as $\langle \dots \rangle$.

III. STATIC EQUATIONS AND HELICAL SOLUTIONS

For a filament with large k and k_3 or at a low T , we can ignore thermal effect and find stable configuration by minimizing E . Extremizing E results in the following static equations:

$$\frac{\partial \mathcal{E}}{\partial \theta} - \frac{d}{ds} \frac{\partial \mathcal{E}}{\partial \dot{\theta}} = \frac{\partial \mathcal{E}}{\partial \psi} - \frac{d}{ds} \frac{\partial \mathcal{E}}{\partial \dot{\psi}} = 0. \quad (9)$$

Explicitly, they are

$$\begin{aligned} 4\ddot{\theta} + 4(c_0 \sin \psi - k_3 \cos 2\theta)\dot{\psi} + (1 - k_3) \sin 4\theta \\ + 2 \sin 2\theta (2c_0 \sin \psi - 1) + 4k_3 \omega_{30} \cos 2\theta = 0, \end{aligned} \quad (10)$$

$$k_3 \ddot{\psi} + (k_3 \cos 2\theta - c_0 \sin \psi)\dot{\theta} + c_0 \sin^2 \theta \cos \psi = 0. \quad (11)$$

For convenience in numerical calculation, we let $R = 1$ and $k = 1$ in Eqs. (10) and (11). Equations (10) and (11) are nonlinear differential equations so that in general they have multiple solutions but it is very difficult to find their general solutions. However, it is easy to obtain the helical solution since owing to symmetry, a helix in the model implies to take $\theta = \theta_h$ as a s -independent constant. Without loss of generality, we let $\pi/2 \geq \theta_h \geq 0$ so $\sin 2\theta_h \geq 0$ and define $z_r \equiv z(L)/L$ so $z_r = \cos \theta_h$ for a helix. The pitch is the height of one complete helix turn measured along the axis of helix so is proportional to z_r .

At $c_0 = \omega_{30} = 0$, the unique GSC of the filament is a straight cylinder [10]. Moreover, when $c_0 = 0$, $\omega_{30} \neq 0$ and $\theta = \theta_h$, from Eqs. (7)–(11), it is straightforward to find that the twist energy is zero and θ is decoupled from ψ so we reach the same result as that at $c_0 = \omega_{30} = 0$.

However, finite c_0 and ω_{30} result in remarkably different results. Taking $\theta = \theta_h$, we can find that either $\psi = \psi_h = \pi/2$ or $3\pi/2$ gives a solution for Eqs. (10) and (11), and let $v = \cos 2\theta_h = 2z_r^2 - 1$, Eqs. (7)–(10) become

$$A = [(1 - k_3)v \pm 2c_0 - 1]\sqrt{1 - v^2} + 2k_3 \omega_{30} v = 0, \quad (12)$$

$$\mathcal{E}_h = \frac{1}{2} \left[k_3 \left(\omega_{30} - \frac{\sqrt{1 - v^2}}{2} \right)^2 + \left(\pm c_0 - \frac{1 - v}{2} \right)^2 \right]. \quad (13)$$

The negative sign before c_0 is due to $\psi_h = 3\pi/2$. However, exact calculations show that $\psi_h = 3\pi/2$ always results in a rather large \mathcal{E}_h and stability analysis reveals that it always gives a unstable state, and similarly there is not bistable helices when $\omega_{30} < 0$. Therefore, we will ignore the cases with $\psi_h = 3\pi/2$ and $\omega_{30} < 0$ henceforth. Equation (12) also confirms that Eqs. (10) and (11) must have multiple solutions.

IV. STABILITY CRITERION

Excluding $\psi_h = 3\pi/2$, Eq. (12) still has four solutions for v but physically v must be a real number. Even v is real, the helix can be still unstable since it can correspond to either a maximum or a saddle point in E . To examine stability of a helix, we linearize Eqs. (10) and (11) by setting $\theta = \theta_h + \Delta\theta$, $\psi = \psi_h + \Delta\psi$ and keeping the terms up to the first order to obtain

$$\ddot{\Delta\theta} + (c_0 - k_3 v)\dot{\Delta\psi} + G\Delta\theta = 0, \quad (14)$$

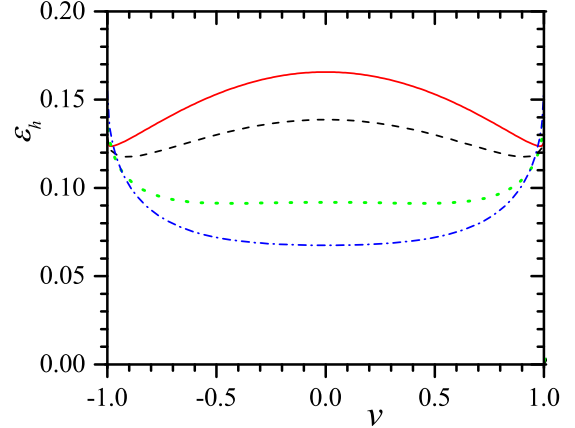


FIG. 1. \mathcal{E}_h vs v when $c_0 = 0.5$, $k_3 = 1.5$ and $\omega_{30} = 0.03$ (solid red), 0.07 (black dashed), 0.15 (green dotted), and 0.2 (blue dash-dotted). Reduced units are used.

$$2k_3 \ddot{\Delta\psi} + 2(k_3 v - c_0)\dot{\Delta\theta} - c_0(1 - v)\Delta\psi = 0, \quad (15)$$

$$G = (2c_0 - 1)v + (1 - k_3)(2v^2 - 1) - 2k_3 \omega_{03} \sqrt{1 - v^2}. \quad (16)$$

Substituting $\Delta\theta = B_\theta e^{\gamma s + \delta}$ and $\Delta\psi = B_\psi e^{\gamma s + \delta}$ into Eqs. (14) and (15), we obtain two linear and s -independent equations for B_θ and B_ψ , and demanding nonvanishing B_θ and B_ψ leads to

$$(\gamma^2 + G)[2k_3 \gamma^2 - c_0(1 - v)] - 2(c_0 - k_3 v)^2 \gamma^2 = 0. \quad (17)$$

Equation (17) is a quadratic equation of γ^2 . If both $\gamma^2 < 0$, then the helix is at least metastable since all γ 's are imaginary so $\Delta\theta$ and $\Delta\psi$ will keep small or it gives either a global or local minimum E ; otherwise, the helix is unstable since at least one $\text{Re}(\gamma^2) > 0$ so it will deviate considerably from a helix at a large s even both B_θ and B_ψ are small. Therefore, γ^2 can be used as stability criterion to justify stability of a helix.

V. BISTABILITY

A. When $c_0 = 0.5$

A very intriguing case occurs at $c_0 = 0.5$. In this case, $A = 0$ has three real solutions, $v = v_1 = 0$, $v = v_{2,3} = \pm \sqrt{(k_3 - 1)^2 - 4k_3^2 \omega_{03}^2 / (k_3 - 1)}$ with $k_3 > 1$. \mathcal{E}_h is the same at both $v = v_{2,3}$, i.e., $v = v_{2,3}$ offer two isoenergetic helices. Clearly, $z_{r,2} = \sqrt{(1 + v_2)/2} > z_{r,3} = \sqrt{(1 + v_3)/2}$. It is easy to show exactly that at least one γ^2 is positive when $v = v_1$ so that the correspond helix is unstable. In contrast, with appropriate ω_{03} we can find $\gamma^2 < 0$ at both $v = v_{2,3}$ so it gives a BS with two distinctive helices.

The typical relationships between \mathcal{E}_h and v when $k_3 = 1.5$, $\omega_{30} = 0.03, 0.07, 0.15$, and 0.2 are presented in Fig. 1. From Fig. 1, we can find that when ω_{30} is small, \mathcal{E}_h has clearly a maximum at $v = v_1$ and two minima at $v = v_{2,3}$, and the larger the ω_{30} , the smaller the $|v_{2,3}|$, shown as the red, black, and green lines in Fig. 1. When $\omega_{30} = 0.15$, \mathcal{E}_h is almost flat, shown as the green line in Fig. 1. Moreover, there is no longer

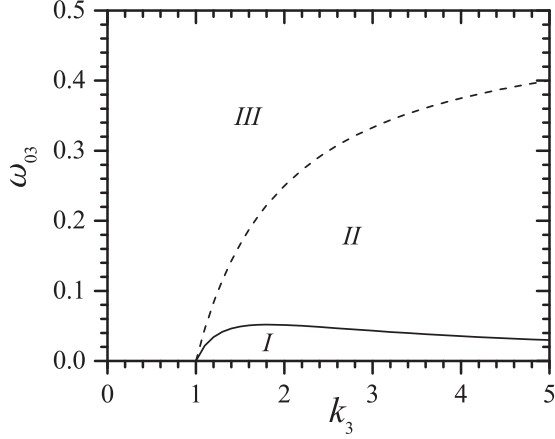


FIG. 2. Phase diagram for stable helix at $c_0 = 0.5$. The solid line and k_3 axis enclose regime *I* in which two helices are stable. The solid and dashed lines enclose regime *II* in which it has a metastable low-pitch helix. The dashed line is given by $\omega_{03} = (k_3 - 1)/2k_3$. Helix is unstable in regime *III* which is above k_3 axis and dashed line. Reduced units are used.

minimum at $\omega_{30} = 0.2$, shown as the blue line in Fig. 1. In a word, two isoenergetic helices can coexist up to a moderate ω_{30} . However, we should indicate that the existence of minimum in \mathcal{E}_h only offers a necessary condition for stability since it ignores effects of either s or ψ . It requires to analyze γ^2 to obtain the sufficient condition for a stable helix.

Figure 2 displays the phase diagram for stability of a helix obtained from analyzing γ^2 . The diagram contains three regimes. Regime *I* is enclosed by k_3 axis and solid line which defines the critical ω_{03} and is obtained from $\gamma^2 = 0$ at both $v = v_{2,3}$. In regime *I*, $\gamma^2 < 0$ at both $v = v_{2,3}$ so that two helices are at least metastable and Monte Carlo simulation reveals that they are stable. In this regime, $\omega_{03} \ll c_0$ and critical $\omega_{03} \rightarrow 0$ slowly with $k_3 \rightarrow \infty$, so that $z_{r,2} \sim 1$ but $z_{r,3} \sim 0$, i.e., two helices are clearly distinguishable. The maximum critical $\omega_{03} \approx 0.052$ occurs at $k_3 \approx 1.8$. Regime *II* is enclosed by the solid and dashed lines which is given by $\omega_{03} = (k_3 - 1)/2k_3 < c_0$ obtained from $\gamma^2 = 0$ at $v = v_3$. In this regime, $\gamma^2 < 0$ at $v = v_3$ so that the low-pitch helix is either stable or metastable, but at $v = v_2$ the helix is unstable. Recalling that two helices have the same \mathcal{E}_h , we can conclude that in regime *II* the GSC is no longer a helix and the low-pitch helix must be metastable. In other words, in both regimes *I* and *II* we can find BS though in regime *II* there is only one metastable low-pitch helix. Regimes *I* and *II* also share the same starting point at $k_3 = 1$. Regime *III* is above k_3 axis and dashed line, and in this regime a helix is unstable due to a small k_3 or a large ω_{03} .

Figures 3 and 4 present relationships between z_r and ω_{30} in regime *I* at $k_3 = 1.2, 1.5, 2.0,$ and 2.5 and exhibit some common behaviors at various parameters. At first, z_r depends on both k_3 and ω_{30} so it is considerably different from that in free space in which z_r or θ_h is independent of k_3 and the unique GSC is a low-pitch helix since $\omega_{30} \ll c_0$. Moreover, z_r of low-pitch helix increases with increasing ω_{30} but decreases with increasing k_3 , and z_r of high-pitch helix shows opposite tendency. Meanwhile, for high-pitch helix

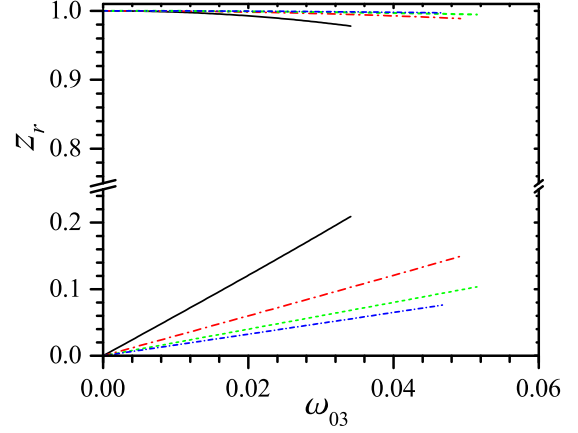


FIG. 3. z_r vs ω_{30} in regime *I* when $c_0 = 0.5$, $k_3 = 1.2$ (solid black), 1.5 (red dash-dotted), 2.0 (green short dashed), and 2.5 (blue short dash-dotted). Reduced units are used.

$z_r \sim 1$ and different k_3 makes little difference in z_r so that for clarification we plot the enlargement of the high-pitch part in Fig. 4, together with two isoenergetic helices of the same $L = 19$. Note that the high-pitch helix (magenta dashed) in Fig. 4 has only 0.27 turn so it does not look like a helix in the figure, but the low-pitch one has 3 turns. In all figures of this paper we use the same color for the data with the same parameters.

B. When $c_0 = 0.45$

When $c_0 \neq 0.5$, there is no longer isoenergetic helices since different roots of Eq. (12) lead to different energies. However, from the sign of γ^2 we can still find BS when $c_0 \approx 0.5$.

We find that when $c_0 < 0.5$, the phase diagram obtained from analyzing γ^2 is divided into four regimes and a typical phase diagram at $c_0 = 0.45$ is displayed in Fig. 5. Regime *I'* has bistable helices with a small ω_{30} and in this regime the high-pitch helix has a lower \mathcal{E}_h so is more stable. Note that

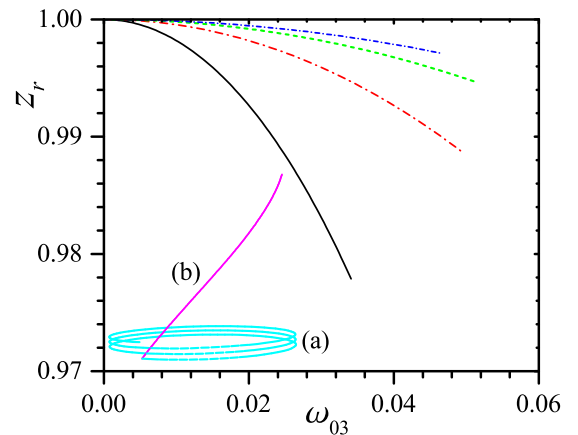


FIG. 4. Enlargement of high-pitch part in Fig. 3 and two isoenergetic helices, i.e., curves (a) and (b), when $k_3 = 1.5$, $\omega_{30} = 0.03$, $L = 19$, $z_r = 0.0905$ (cyan dashed and 3 turns), and $z_r = 0.9959$ (solid magenta and 0.27 turn). Reduced units are used.

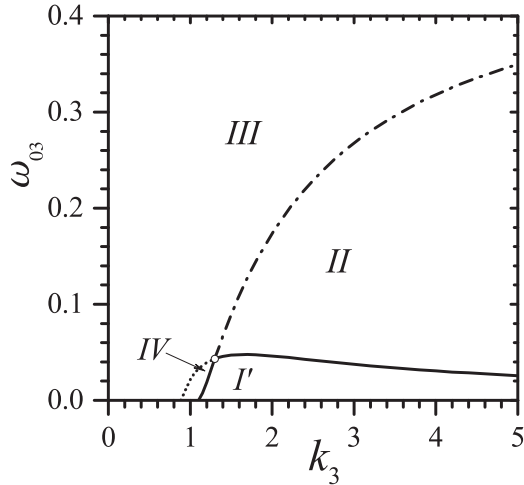


FIG. 5. Phase diagrams for stable helix when $c_0 = 0.45$. Regime I' is bound by solid line and has bistable helices. Regime II is bound by solid and dash-dotted lines and has a metastable low-pitch helix. Regime III is above dash-dotted and short dotted lines and a helix is unstable in this regime. Regime IV has a metastable high-pitch helix and is bound by short dotted and solid lines. The empty circle is at $k_3 \approx 1.3$, $\omega_{30} = 0.043$ and denotes the end of dotted line as well as the start of dash-dotted line. Reduced units are used.

two helices are no longer isoenergetic in regime I' so we use a different symbol from that at $c_0 = 0.5$ to label the regime. Similar to that at $c_0 = 0.5$, in regime II there is a metastable low-pitch helix since it has a higher \mathcal{E}_h than that of the high-pitch unstable helix, so that BS still exists in the regime. Both regimes I' and II require $k_3 > 1$ but regime II starts at a larger $k_3 > 1$ but regime II allows $k_3 < 1$ so they have not a common starting k_3 , as shown in Fig. 5 in which the empty circle gives the starting k_3 for regime II . Again and the same as that at $c_0 = 0.5$, helix is unstable in regime III . Moreover, regime IV allows $k_3 < 1$ and has a small range, exists only when $c_0 < 0.5$ and there is a stable or metastable high-pitch helix since it has a lower \mathcal{E}_h than that of the low-pitch unstable helix so this regime is clearly different from other three regimes. We cannot determine directly whether BS exists in regime IV since we cannot decide whether the high-pitch helix is GSC, but it should be similar more to regime II .

Figures 6 and 7 display the relationships between z_r , \mathcal{E}_h , and ω_{30} in regimes I' when $c_0 = 0.45$, $k_3 = 1.2, 1.5$, and 2.5 . The basic properties are similar to that at $c_0 = 0.5$. From Figs. 6 and 7, we know that when $c_0 < 0.5$, the high-pitch helix with $\mathcal{E}_h = \mathcal{E}_2$ is more stable since it has a lower \mathcal{E}_h than that of the low-pitch helix with $\mathcal{E}_h = \mathcal{E}_3$. Moreover, similar to that at $c_0 = 0.5$, z_r of high-pitch helix is very close to 1 and decreases slightly with increasing c_0 . We find that when $c_0 < 0.5$, z_r of high-pitch helix is more close to 1 than that at $c_0 = 0.5$ so that without a proper enlargement it is very difficult to distinguish them according to the value of k_3 , as shown in Fig. 6. Therefore, in Fig. 7 we replot the enlarged high-pitch part in Fig. 6, together with two bistable helices of the same k_3 and ω_{30} as that in Fig. 4. The high-pitch helix in Fig. 7 has only 0.15 turn, much smaller than its counterpart in Fig. 4. \mathcal{E}_h are nearly overlapped at different k_3 and ω_{30} owing to a small ω_{30} , shown as \mathcal{E}_2 and \mathcal{E}_3 in Fig. 6.

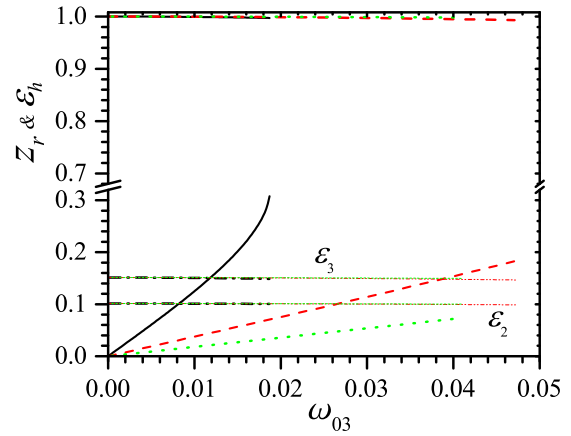


FIG. 6. z_r and \mathcal{E}_h vs ω_{30} in regime I' when $c_0 = 0.45$, $k_3 = 1.2$ (solid black line for z_r and black dash-dotted line for \mathcal{E}_h), 1.5 (red dashed line for z_r and red dash-dot-dotted line for \mathcal{E}_h), and 2.5 (green dotted line for z_r and green short dashed line for \mathcal{E}_h). \mathcal{E}_2 is the energy for high-pitch helix and \mathcal{E}_3 is the energy for low-pitch helix at the same k_3 . Reduced units are used.

C. When $c_0 = 0.55$

When $c_0 > 0.5$ there are only three regimes in phase diagram for stable helix. Figure 8 displays a typical phase diagram at $c_0 = 0.55$. In regime I' , there are bistable helices but the low-pitch helix is more stable so is different from that at $c_0 \leq 0.5$. Regime II is similar to that at $c_0 \leq 0.5$ since there is only one metastable low-pitch helix. Moreover, helix is also unstable in regime III . When $c_0 > 0.5$, regime I' requires $k_3 > 1$ but regime II allows $k_3 < 1$ so they have not a common starting k_3 . Moreover, comparing Figs. 2, 5, 8, we can find that the larger the c_0 , the larger the range of regimes I' and II .

Figure 9 displays the relationships between z_r , \mathcal{E}_h , and ω_{30} in regimes I' when $c_0 = 0.55$, $k_3 = 1.2, 1.5$, and 2.5 . The basic properties are also similar to that at $c_0 = 0.5$. In Sec. VB we point out that when $c_0 < 0.5$, the high-pitch helix is more stable since it has a lower \mathcal{E}_h than that of the low-pitch helix.

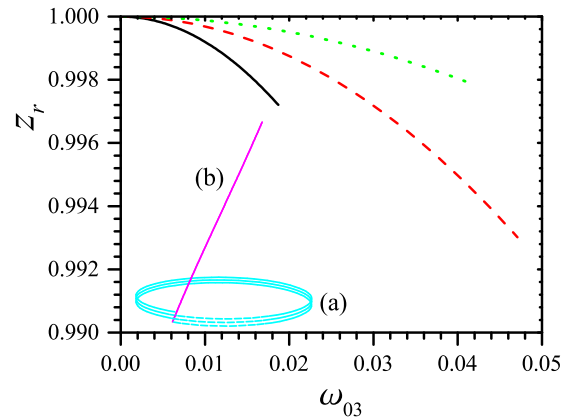


FIG. 7. Enlargement of high-pitch part of Fig. 6 and two bistable helices, i.e., curves (a) and (b), in regime I' when $k_3 = 1.5$, $\omega_{30} = 0.0303$, $L = 19$, $z_r = 0.0543$ (cyan dashed and 3 turns, $\mathcal{E} = 0.1504$), and $z_r = 0.9989$ (solid magenta and 0.15 turn, $\mathcal{E} = 0.1006$). Reduced units are used.

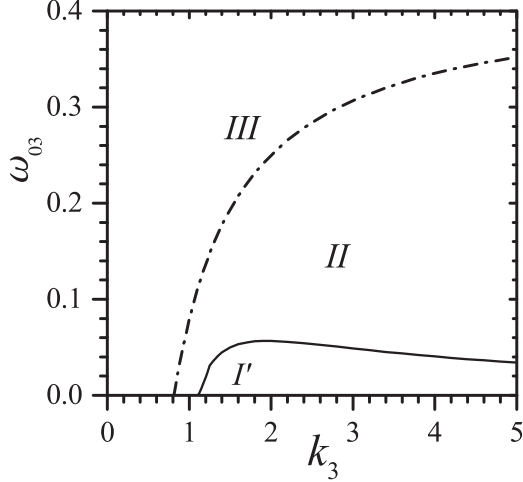


FIG. 8. Phase diagrams for stable helix when $c_0 = 0.55$. Three regimes have the same meaning as that in Fig. 5. Reduced units are used.

However, when $c_0 > 0.5$, the low-pitch helix with $\mathcal{E}_h = \mathcal{E}_3$ becomes more stable since it has a lower \mathcal{E}_h than that of the high-pitch helix, as shown in Fig. 9. Moreover, similar to that at $c_0 = 0.5$, z_r of high-pitch helix is close to 1 but decreases slightly with increasing c_0 . Again, \mathcal{E}_h are nearly overlapped at different k_3 and ω_{30} , shown as \mathcal{E}_2 and \mathcal{E}_3 in Fig. 9.

Comparing Figs. 3, 6, 9, we can find that the larger the c_0 , the smaller the z_r for a low-pitch helix. Similarly, we can see that the smaller the c_0 , the smaller the difference between z_r of two helices at the same BS owing to the larger z_r at low-pitch case.

D. Three regimes in terms of k_3 and c_0

We find further that a large k_3 and a moderate c_0 favor helix, as shown in Fig. 10. The boundaries of three regimes in Fig. 10 are given by $k_3 = 2c_0$ and $k_3 = 2 - 2c_0$. The solid

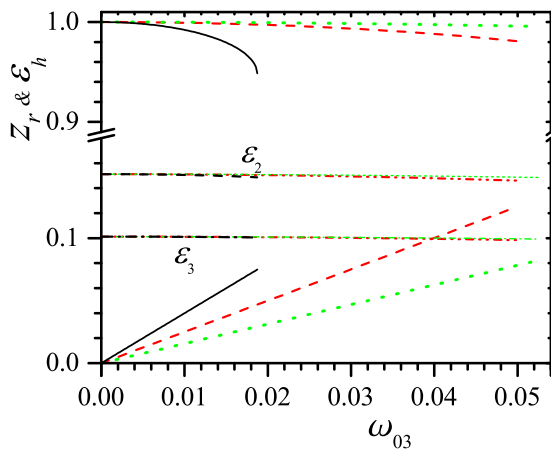


FIG. 9. z_r and \mathcal{E}_h vs ω_{30} in regime I' when $c_0 = 0.55$, $k_3 = 1.2$ (solid black line for z_r and black dash-dotted line for \mathcal{E}_h), 1.5 (red dashed line for z_r and red dash-dot-dotted line for \mathcal{E}_h), and 2.5 (green dotted line for z_r and green short dashed line for \mathcal{E}_h). \mathcal{E}_2 and \mathcal{E}_3 have the same meaning as that in Fig. 6. Reduced units are used.

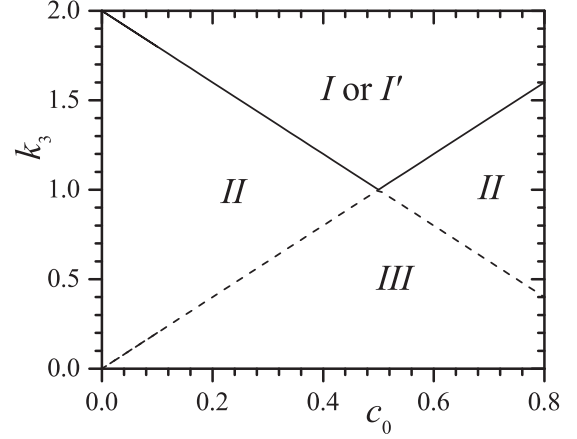


FIG. 10. Three regimes in terms of k_3 and c_0 . There are bistable helices in regime I or I' bound by solid lines. It has only one stable or metastable helix in regime II bound by solid and dashed lines. There is no stable helix below dashed lines which defines regime III . Two straight lines are given by $k_3 = 2c_0$ and $k_3 = 2 - 2c_0$. Three regimes have the same meaning as that in Figs. 2 and 5. Reduced units are used.

line is obtained from $\gamma^2 = 0$ at both $v = v_{2,3}$ and the dashed line is obtained from $\gamma^2 = 0$ at either $v = v_2$ or $v = v_3$. Note that regime II in Fig. 10 includes regime IV in Fig. 5.

Our results reveal that c_0R plays a key role for the formation of BS and it is a natural result since it represents the competition and cooperation between intrinsic property and geometric confinement, and this is also why one of bistable helices is close to a straight cylinder and the other is close to a circle. However, a finite ω_{03} favors a large z_r so that to have a BS it requires both a finite ω_{03} and a large k_3 .

VI. SIMULATION RESULTS

To verify whether a helix is in ground state and whether above exact results are also valid for a discrete short chain, we perform MC simulation to some short chains when $c_0R = 0.5$.

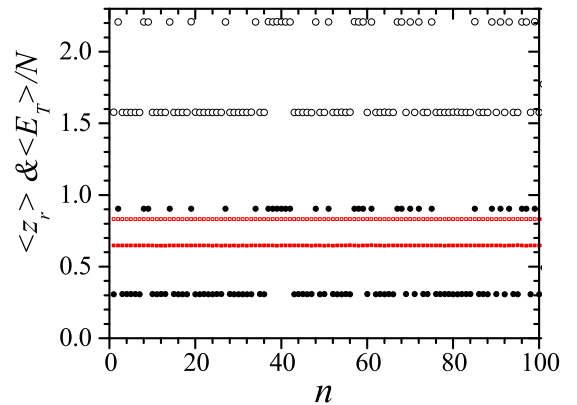


FIG. 11. $\langle z_r \rangle$ (solid) and $\langle E_T \rangle / N$ (empty) vs sample counts when $c_0R = 0.5$, $R = 3$, $N = 20$, $b = 80$ (black circle) or 10 (red square), $b_3/b = 1.5$, and $\omega_{03}R = 0.03$ (in regime I). The percentage of high-pitch helices in the figure is 31%. Reduced units are used.

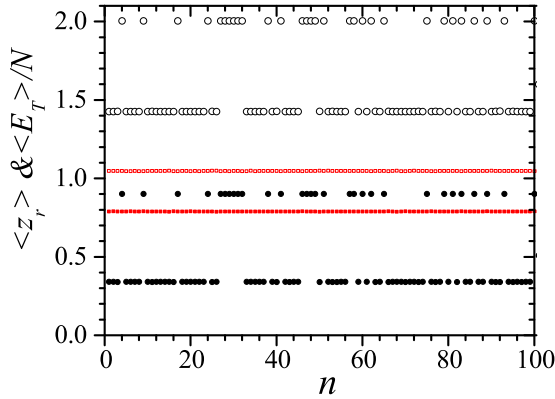


FIG. 12. $\langle z_r \rangle$ (solid) and $\langle E_T \rangle/N$ (empty) vs. sample counts when $c_0R = 0.5$, $R = 3$, $N = 20$, $b = 80$ (black circle) or 20 (red square), $b_3/b = 1.5$, and $\omega_{03}R = 0.1$ (in regime *II*). The percentage of high-pitch helices in the figure is 30%. Reduced units are used.

Figures 11–14 show some typical results for $\langle z_r \rangle$ and $\langle E_T \rangle/N$ of 100 samples when $N = 20$, $R = 3$, $b = 10$ (red square), 20 (red square), 50 (red square), 80 (black circle), $b_3/b = 1.5$, $\omega_{03}R = 0.03$ (in regime *I*), 0.1 (in regime *II*), and 0.5 (in regime *III*). In these figures, we use the same symbol to represent samples having the same parameters (N , R , b , b_3 and ω_{03}) but different initial configurations. From black solid circles in Figs. 11–13, we can see that when b ($=80$) and b_3 are sufficient large, $\langle z_r \rangle$ of the same parameters has indeed two distinct values and the magnitude of larger z_r is close to 1. Meanwhile, the larger the $\omega_{03}R$, the smaller the difference between two $\langle z_r \rangle$'s. It confirms exact results in regime *I* and *II*, i.e., in regime *I* two helices in the same BS are GSCs and in regime *II* the low-pitch helix is at least metastable. Simulation results also suggest that there is not any other stable configuration than helices in regime *I* and the stability analysis in last section is also valid for a short filament.

$\langle z_r \rangle$ in simulation is slightly different from z_r obtained in Sec. V, but increasing b and b_3 can improve the agreement and it is a natural result since GSC is the limit at $T = 0$ or at $b \rightarrow \infty$ and $b_3 \rightarrow \infty$. Moreover, even at large b ($=80$) and

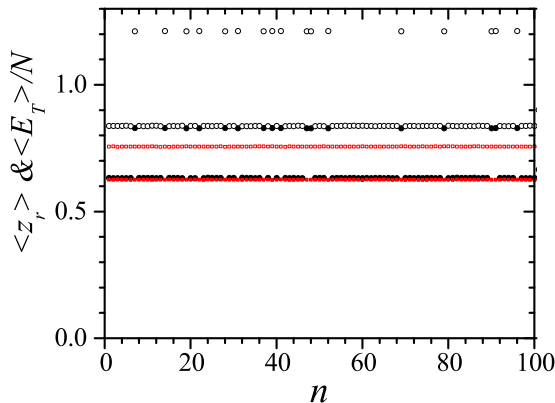


FIG. 13. $\langle z_r \rangle$ (solid) and $\langle E_T \rangle/N$ (empty) vs. sample counts when $c_0R = 0.5$, $R = 3$, $N = 20$, $b = 80$ (black circle) or 50 (red square), $b_3/b = 1.5$, and $\omega_{03}R = 0.5$ (in regime *III*). The percentage of high-pitch helices in the figure is 17%. Reduced units are used.

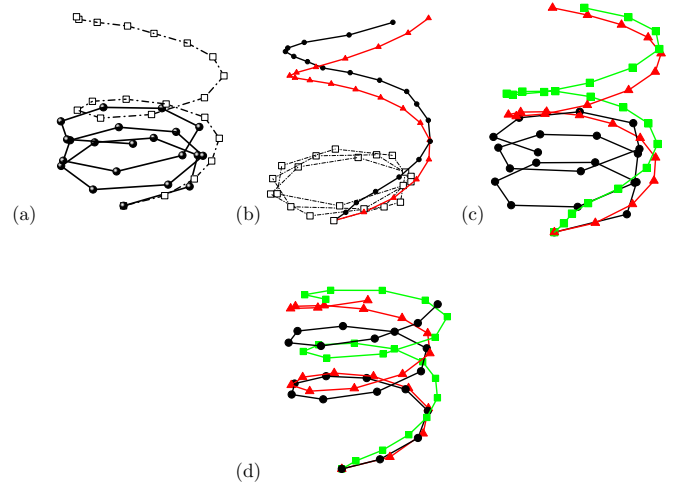


FIG. 14. Snapshots of some samples when $c_0R = 0.5$, $R = 3$, $N = 20$, $b = 80$, $b_3/b = 1.5$, and (a) $\omega_{03}R = 0.03$ and $\langle z_r \rangle = 0.3065$. The dash-dotted line with empty square is the initial configuration (MCS = 0) with $z_r = 0.8023$; the solid line with circle is the snapshot of the same sample at MCS = 1.5×10^7 . (b) $\omega_{03}R = 0.03$ and $\langle z_r \rangle = 0.9036$. The black dash-dotted line with empty square is the initial configuration with $z_r = 0.0826$; the black solid line with circle is the snapshot of the same sample at MCS = 1.5×10^7 , the red line with triangle is a helix obtained by averaging the snapshot. (c) $\omega_{03}R = 0.1$, MCS = 1.5×10^7 , $\langle z_r \rangle = 0.3392$ (black solid line with circle) and 0.9005 (green solid line with square), the red line with triangle is a helix obtained by averaging the snapshot with $\langle z_r \rangle = 0.9005$. (d) $\omega_{03}R = 0.5$, MCS = 1.5×10^7 , $\langle z_r \rangle = 0.6322$ (black solid line with circle) and 0.8285 (green solid line with square), the red line with triangle is a helix obtained by averaging the snapshot with $\langle z_r \rangle = 0.8285$. Reduced units are used.

b_3 , two $\langle E_T \rangle$'s in the same BS are still different in all three regimes and the sample with a larger $\langle z_r \rangle$ has a higher $\langle E_T \rangle$, shown as empty symbols in Figs. 11–13. This result disagrees with exact calculations, but two $\langle E_T \rangle$'s tend to close to each other with increasing b and b_3 so the disagreement is also a thermal effect. Thermal fluctuation also leads to that fewer samples in the same BS can stay in the configuration with a large $\langle z_r \rangle$ since it has a higher $\langle E_T \rangle$, as shown in Figs. 11–13. In fact, when b or b_3 is sufficient small, simulation outputs a single $\langle z_r \rangle$ only or we can no longer observe BS, shown as red circles in Figs. 11–13 with $b = 10$, 20, and 50. This is because the energy barrier between two configurations in a same BS must be smaller than or comparable to $k_B T$ so that the filament shifts frequently between two configurations. At moderate b and b_3 , we can even observe several different $\langle z_r \rangle$'s in simulation and it must be due to that the energy barrier is close to $k_B T$ so the system relaxes very slowly and leads to a scattered average. Simulation results also indicate that in regime *I* it is relative easier to find BS, i.e., it requires smaller b and b_3 to obtain a single $\langle z_r \rangle$, as shown in Figs. 11–13. All in all, at a finite T it requires sufficient large b and b_3 to keep the filament staying at one of two configurations in a BS because in this case the energy barrier between two configurations is larger than $k_B T$.

A little surprised we find that BS also exists in regime *III*, as shown in Fig. 13. It is out of anticipation from exact

calculations and suggests that there are bistable nonhelices in regime *III*. Owing to thermal effect, we cannot determine whether the BS in this regime is energetically degenerate. Moreover, we should point out that in this case, the difference between two $\langle z_r \rangle$'s in a BS is relative small and it is rather sensitive to magnitudes of b and b_3 . For instance, from Fig. 13 we can see that keeping b_3/b unchanged but decreasing b from 80 (black circle) to 50 (red square) is enough to yield a single $\langle z_r \rangle$.

Figure 14 shows some snapshots for bistable configurations at $MCS = 0$ (initial configuration) or 1.5×10^7 and with the same parameters (except for those with $b < 80$) as that in Figs. 11–13. Examining initial configurations we find that the final configuration tends to close to the initial one, but it is not always so, as shown in Figs. 14(a) and 14(b). In Fig. 14(a), the initial configuration (dash-dotted line with empty square) has $z_r = 0.8023$ so is closer to that of the high-pitch one of the same parameters as shown in Fig. 14(b), but the snapshot is a low-pitch one and $\langle z_r \rangle = 0.3065$. In contrast, in Fig. 14(b), the initial configuration (dash-dotted line with empty square) has $z_r = 0.0826$ so is closer to that of the low-pitch one, but the snapshot is a high-pitch one and $\langle z_r \rangle = 0.9036$. This is again a thermal effect so that large b and b_3 can prevent such a behavior. We also find that more samples with large initial z_r have such a behavior and this is a natural result since they have a higher $\langle E_T \rangle$. The thermal fluctuation also leads to difficult in setting a proper standard to justify whether the snapshot with a small z_r is a helix so we do not display the mean configuration for them, but for the snapshot with a large z_r , from Figs. 14(b)–14(d) we can see that the larger the $\omega_{03}R$, the larger the deviation from a helix, especially note that in Fig. 14(d) the snapshot in green-solid-line with square is clearly different from its mean helix, i.e., the red line with triangle. It supports the stability analysis in Sec. V, i.e., a high-pitch helix is unstable in either regimes *II* or *III*. Moreover, in both regimes *I* and *II*, the low-pitch snapshots are clearly distinguishable from the high-pitch ones, as we can see from Figs. 14(a)–14(c). However, in regime *III* it is difficult to distinguish snapshots of two configurations though they still have clearly different $\langle z_r \rangle$, as shown in Fig. 14(d), so it suggests that to distinguish them requires much larger b and b_3 than that in regimes *I* and *II*.

Simulation results indicate that when b or b_3 is small, the system can be used as an oscillator since it tends to shift frequently between two configurations. In contrast, with large

b and b_3 the system can be used to make memory or switch or energy storage material or display. In practice, the values of b and b_3 can be changed by either changing T or both k and k_3 . Finally, the simulation results also suggest that the static equations of the system has only two stable or metastable solutions and in regime *I* or *I'* helices give GSCs of the system.

VII. CONCLUSIONS AND DISCUSSIONS

In summary, we show exactly that confining an intrinsically curved and twisted filament on a cylinder can create a bistable material. Using standard variational technique first we derive static equations for stable configurations of system and find the closed-form expressions for helical solution, and then we linearize static equations around the helical solution to obtain closed-form stability criterion for a helix. We find that the key parameter for bistability of a helix is c_0R since it reflects competition and cooperation between intrinsic property and geometric constraint. When $c_0R = 0.5$ and $k_3 > k_1$, the phase diagram for stability of helices is divided into three regimes. Regime *I* has a small ω_{30} and exists a BS which consists of two isoenergetic helices. In regime *II*, the filament has a moderate ω_{30} and BS consists of a metastable helix and a stable nonhelix. In regime *III*, large ω_{30} prevents stable helix. Similar results are observed when $c_0R \sim 0.5$ though there is no longer isoenergetic helices. Monte Carlo simulation confirms these conclusions and suggests further that there are bistable nonhelices in regime *III*.

Some significant advantages can facilitate the realization and application of this BS system. First, it offers a potential green material since it does not need external force to keep the system staying in one of two configurations in a BS. Second, it allows an arbitrary length of filament and has a wide range in parameters so is rather flexible for choosing appropriate materials in application. In particular, the requirement of a small ω_{30} for BS can be removed by applying a torque or binding the cross-section in ends to obtain a small effective ω_{30} . Third, distinctive pitches in BS makes it be easier to detect or control. Moreover, helix is a chiral system so that the bistable system provides a promising optically active material. More exactly, in regime *I* the transition between two distinctive helices may yield variable colors; and in regime *II*, the helix-nonhelix transformation may also lead to novel optical property. Finally, our findings must be instructive to other confined systems.

-
- [1] Y.-C. Wang and E. L. Ferguson, *Nature (London)* **434**, 229 (2005).
 - [2] H. Shin, S. Seo, C. Park, J. Na, M. Han, and E. Kim, *Energy Environ. Sci.* **9**, 117 (2016).
 - [3] W. Zhang, X. Wang, Y. Wang, G. Yang, C. Gu, W. Zheng, Y.-M. Zhang, M. Li, and S. X.-A. Zhang, *Nat. Commun.* **10**, 1559 (2019).
 - [4] Y. Wang, S. Wang, X. Wang, W. Zhang, W. Zheng, Y.-M. Zhang, and S. X.-A. Zhang, *Nat. Mater.* **18**, 1335 (2019).
 - [5] F. Tanaka and H. Takahashi, *J. Chem. Phys.* **83**, 6017 (1985).
 - [6] B. Fain, J. Rudnick, and S. Östlund, *Phys. Rev. E* **55**, 7364 (1997).
 - [7] B. Fain and J. Rudnick, *Phys. Rev. E* **60**, 7239 (1999).
 - [8] S. V. Panyukov and Y. Rabin, *Phys. Rev. E* **64**, 011909 (2001).
 - [9] Z. Zhou, P.-Y. Lai, and B. Joós, *Phys. Rev. E* **71**, 052801 (2005).
 - [10] Z. Zhou, *J. Phys. Comm.* **2**, 035008 (2018).
 - [11] J. F. Marko and E. D. Siggia, *Science* **265**, 506 (1994).
 - [12] J. Moukhtar, E. Fontaine, C. Faivre-Moskalenko, and A. Arnéodo, *Phys. Rev. Lett.* **98**, 178101 (2007).

- [13] H. Yamakawa and T. Yoshizaki, *Helical Wormlike Chains in Polymer Solutions* (Springer-Verlag, Berlin, 1996).
- [14] A. Goriely and P. Shipman, *Phys. Rev. E* **61**, 4508 (2000).
- [15] B. Smith, Y. V. Zastavker, and G. B. Benedek, *Phys. Rev. Lett.* **87**, 278101 (2001).
- [16] D. A. Kessler and Y. Rabin, *Phys. Rev. Lett.* **90**, 024301 (2003).
- [17] J. L. Marin, R. Riera, and R. A. Rosas, *Handbook of Advanced Electronic and Photonic Materials and Devices*, Vol. 6: Nanostructured Materials, edited by H. S. Nalwa (Academic Press, Boston, MA, 2001).
- [18] K. S. Novoselov, A. K. Geim, S. V. Morozov, D. Jiang, Y. Zhang, S. V. Dubonos, I. V. Grigorieva, and A. A. Firsov, *Science* **306**, 666 (2004).
- [19] S. Manzeli, D. Ovchinnikov, D. Pasquier, O. V. Yazyev, and A. Kis, *Nat. Rev. Mater.* **2**, 17033 (2017).
- [20] N. Mounet, M. Gibertini, P. Schwaller, D. Campi, A. Merkys, A. Marrazzo, T. Sohier, I. E. Castelli, A. Cepellotti, G. Pizzi, and N. Marzari, *Nat. Nanotechnol.* **13**, 246 (2018).
- [21] S. C. Bae, F. Xie, S. Jeon, and S. Granick, *Curr. Opin. Solid State Mater. Sci.* **5**, 327 (2001).
- [22] B. Maier, U. Seifert, and J. O. Radler, *Europhys. Lett.* **60**, 622 (2002).
- [23] D. A. Matoz-Fernandez, D. H. Linares, and A. J. Ramirez-Pastor, *Europhys. Lett.* **82**, 50007 (2008).
- [24] P. Longone, D. H. Linares, and A. J. Ramirez-Pastor, *J. Chem. Phys.* **132**, 184701 (2010).
- [25] D. R. Tree, Y. Wang, and K. D. Dorfman, *Phys. Rev. Lett.* **110**, 208103 (2013).
- [26] S. Schobl, S. Sturm, W. Janke, and K. Kroy, *Phys. Rev. Lett.* **113**, 238302 (2014).
- [27] U. R. Dahal and E. E. Dormidontova, *Phys. Rev. Lett.* **117**, 027801 (2016).
- [28] R. J. Masurel, P. Gelineau, S. Cantournet, A. Dequidt, D. R. Long, F. Lequeux, and H. Montes, *Phys. Rev. Lett.* **118**, 047801 (2017).
- [29] I. Zivic, S. Elezovic-Hadzic, and S. Milosevic, *Phys. Rev. E* **98**, 062133 (2018).
- [30] J. Z. Y. Chen, *Phys. Rev. Lett.* **121**, 037801 (2018).
- [31] T. Curk, J. D. Farrell, J. Dobnikar, and R. Podgornik, *Phys. Rev. Lett.* **123**, 047801 (2019).
- [32] S. Das and A. Cacciuto, *Phys. Rev. Lett.* **123**, 087802 (2019).
- [33] B. Zuo, H. Zhou, M. J. B. Davis, X. Wang, and R. D. Priestley, *Phys. Rev. Lett.* **122**, 217801 (2019).
- [34] Q. Tang, M. Muller, C. Y. Li, and W. Hu, *Phys. Rev. Lett.* **123**, 207801 (2019).
- [35] L. J. F. Jones, R. Carballido-López, and J. Errington, *Cell* **104**, 913 (2001).
- [36] R. A. Daniel and J. Errington, *Cell* **113**, 767 (2003).
- [37] Z. Gitai, N. Dye, and L. Shapiro, *Proc. Natl. Acad. Sci. USA* **101**, 8643 (2004).
- [38] Z. Gitai, N. Dye, A. Reisenauer, M. Wachi, and L. Shapiro, *Cell* **120**, 329 (2005).
- [39] T. Kruse, J. Bork-Jensen, and K. Gerdes, *Mol. Microbiol.* **55**, 78 (2005).
- [40] R. Carballido-López, *Microbiol. Mol. Biol. Rev.* **70**, 888 (2006).
- [41] O. Esue, D. Wirtz, and Y. Tseng, *J. Bacteriol.* **188**, 968 (2006).
- [42] P. Vats and L. Rothfield, *Proc. Natl. Acad. Sci. USA* **104**, 17795 (2007).
- [43] H. P. Erickson, D. W. Taylor, K. A. Taylor, and D. Bramhill, *Proc. Natl. Acad. Sci. USA* **93**, 519 (1996).
- [44] N. Iwai, K. Nagai, and M. Wachi, *Biosci. Biotechnol. Biochem.* **66**, 2658 (2002).
- [45] R. Srinivasan, M. Mishra, M. Murata-Hori, and M. K. Balasubramanian, *Curr. Biol.* **17**, 266 (2007).
- [46] S. van Teeffelen, S. Wanga, L. Furchtgott, K. C. Huang, N. S. Wingreen, J. W. Shaevitz, and Z. Gitai, *Proc. Natl. Acad. Sci. USA* **108**, 15822 (2011).
- [47] C. Reimold, H. J. D. Soufoa, F. Dempwolff, and P. L. Graumann, *Mol. Biol. Cell* **24**, 2340 (2013).
- [48] J. Errington, *Nature Rev. Microbiol.* **13**, 241 (2015).
- [49] N. D. Rochman and S. X. Sun, *Soft Matter* **12**, 779 (2016).
- [50] J. Fierling, A. Johner, I. M. Kulić, H. Mohrbach, and M. M. Müllera, *Soft Matter* **12**, 5747 (2016).
- [51] D. A. Quint, A. Gopinathan, and G. M. Grason, *Biophys. J.* **111**, 1575 (2016).
- [52] Z. Zhou, B. Joós, and C.-X. Wu, *AIP Adv.* **7**, 125003 (2017).
- [53] Z. Zhou, *Phys. Rev. E* **103**, 012410 (2021).
- [54] C. J. Benham, *Proc. Natl. Acad. Sci. USA* **74**, 2397 (1977).
- [55] H. Goldstein, *Classical Mechanics*, 3rd ed. (Addison-Wesley, Boston, MA, 2002).
- [56] Z. Zhou and C.-X. Wu, *Eur. Biophys. J.* **48**, 329 (2019).
- [57] J. F. Allard and A. D. Rutenberg, *Phys. Rev. Lett.* **102**, 158105 (2009).